



Full length article

A model of full thermodynamic stabilization of nanocrystalline alloys



Omar Hussein, Yuri Mishin

Department of Physics and Astronomy, MSN 3F3, George Mason University, Fairfax, VA 22030, USA

ARTICLE INFO

Keywords:

Nanocrystalline material
Alloy
Grain boundary
Thermodynamics
Stability
Monte Carlo

ABSTRACT

We propose a model of a polycrystalline alloy combining the Potts model for grain orientations with a lattice-gas model for solute thermodynamics and diffusion. The alloy evolution with this model is implemented by kinetic Monte Carlo simulations with nonlinear transition barriers between microstates. The model is applied to investigate the long-standing question of whether grain boundary (GB) segregation of an appropriate solute can drive the GB free energy to zero, creating a fully stabilized polycrystalline state with a finite grain size. The model reproduces stable polycrystalline states under certain conditions, provided the solute-solute interactions are repulsive. The material's structure minimizing the total free energy is not static. It exists in a state of dynamic equilibrium between the competing processes of grain growth and grain refinement. The alloy eliminates triple junctions by forming a set of smaller grains embedded into a larger matrix grain. It is predicted that, if a fully stabilized nanocrystalline state is realized experimentally, it will look very different from the conventional (unstable) nanocrystalline materials.

1. Introduction

Over the past decades, nanocrystalline (NC) materials have attracted much attention in both research and technological applications [1,2]. Some mechanical and physical properties of NC materials are superior to those of their conventional, coarse-grained counterparts. However, NC materials are thermodynamically unstable because grain boundaries (GBs) possess an excess free energy relative to the perfect crystalline lattice. This excess free energy causes extensive grain growth at elevated temperatures. Once the grains grow in size well above the nanoscale, the superior properties of the NC material are lost.

Significant research efforts have been dedicated to finding ways to stabilize NC materials against grain growth by alloying with suitable solutes. Two ways to achieve stabilization have been pursued: decreasing the GB free energy γ by GB segregation of appropriate solutes, or reducing the GB mobility. These two strategies are often referred to as the thermodynamic and kinetic stabilization mechanisms.

The basic principle behind the thermodynamic stabilization can be traced back to Gibbs [3]. The Gibbs adsorption equation predicts a reciprocal relation between interface segregation and the reduction in the interface tension. In fact, it is this reduction in free energy that drives the interface segregation. There has been extensive research, both experimental and theoretical, aiming to find solutes that cause significant reduction in the GB free energy. The search was aided by constructing nano-stability diagrams based on thermodynamic calculations for many alloy systems [4–18]. Experimentally, grain growth

retardation by alloying has been demonstrated in numerous alloys, although the extent of the retardation varies. When significant stabilization was achieved, it was not always clear if the success could be attributed to a reduction in γ or suppression of GB mobility. One of the challenges in this approach is that one can only pack that much solute in GBs. After that, the solute atoms start precipitating as a bulk phase.

In the kinetic mechanism, the GB mobility is reduced by the solute drag effect [19–33] or Zener pinning of GBs by small particles [20, 34–42]. A prominent example of extremely strong nano-stabilization is offered by Cu-Ta alloys [35,41–45]. Ta is virtually immiscible in Cu. When a small amount of Ta is forced into Cu by mechanical alloying followed by consolidation and thermal processing, Ta precipitates from the metastable solution as nanoclusters coherent with the Cu matrix. These nanoclusters pin the GBs in place and prevent grain growth. The grains do not grow significantly up to 0.9 of the melting point. This high-temperature NC alloy exhibits extraordinary properties, such as high strength of about a GPa, excellent creep resistance, fatigue endurance, and even shock deformation resistance. Thus, in practical terms, the Zener pinning of GBs is probably the most effective nano-stabilization mechanism known today. Although other approaches, such as solute drag and lowering the GB free energy by segregation, are less effective, they nevertheless present significant fundamental interest.

* Corresponding author.

E-mail address: ymishin@gmu.edu (Y. Mishin).

In the 1990s, Weissmuller [46,47] and later others [4–12,48–54] discussed the possibility of decreasing the GB free energy until the total free energy of the polycrystal reaches a minimum at a *finite* grain size.¹ In the minimum-free-energy state, the driving force for grain growth vanishes, and the NC material becomes *fully stabilized*. Thermodynamic analysis within the uniform boundary model predicts that in order to achieve the fully stabilized state, the GB free energy γ must converge to a zero value when the system arrives at the equilibrium state [55].

This fascinating idea has been debated in the literature for many years. At first sight, it may seem that it contradicts Gibbs' thermodynamics. Gibbs predicted that as long as $\gamma \leq 0$, the material will keep increasing its interface area by breaking into infinitely thin lamellae. However, this thought experiment assumes an open system with unlimited supply of solute atoms to the interfaces. Real nano-grains have a finite capacity to supply the solute to GBs. At some degree of grain refinement, the grains will no longer be able to provide enough solute to sustain the $\gamma \leq 0$ condition. At this point, the process of grain refinement should stop, and the polycrystalline system should reach equilibrium between GB segregation and the solid solution in the grains.

To our knowledge, a fully stabilized state has never been demonstrated experimentally. In addition to the mentioned competition between GB segregation and bulk phase transformations, it might be difficult to distinguish thermodynamic stabilization from kinetic trapping on the experimental time scales. There are also many unanswered fundamental questions surrounding the full stabilization. For example, GB segregation is known to depend on the GB crystallography. Can the $\gamma = 0$ condition be achieved simultaneously at all GBs in a polycrystalline sample? Even if it can, which is unlikely, the triple junction (TJ) free energy does not have to approach zero when GBs do. If the TJ free energy remains positive, a driving force for structural evolution remains, and the polycrystal is not fully stabilized. One can argue that the zero free energy conditions at GBs (or TJs) must be satisfied in an average sense. If so, then what will the stable structure look like if the free energy is positive for some GBs (or TJs) and negative for others? How will such a structure evolve in time? These seemingly abstract questions are linked to the practical question of whether it is worth the efforts to pursue the full stabilization experimentally.

In our previous publication [55], we developed a simple model aiming to address some of the questions mentioned above. The model combines the Ising model on a two-dimensional (2D) lattice with a lattice gas model of a solid solution. It captures the concurrent processes of GB migration and solute diffusion, and is solved by kinetic Monte Carlo (KMC) simulations. The simulations revealed the formation of a stable polycrystalline (more accurately, bicrystalline) state in a certain range of temperatures and chemical compositions. The stable structure is composed of isolated grains nested in one another and dynamic in nature. The grains are constantly growing and shrinking and remain in dynamic equilibrium with each other. As expected, the GB free energy γ computed by thermodynamic integration methods was found to be zero in the equilibrium state.

Although the previous model [55] confirmed the link between the full stabilization and the $\gamma = 0$ condition and provided some glimpse into the possible equilibrium structures, it suffered from significant limitations. The model considered only two crystallographic orientations and could not properly represent a polycrystalline state. Furthermore, the structures could not contain TJs, leaving their role in the stabilization unexplored. In addition, the melting temperature of the single-crystalline state was predicted to be a second-order transition, not a first-order transition as in reality.

In this paper, we expand the previous model by replacing the Ising model with a Potts model [56] capable of representing multiple crystallographic orientations. In Section 2, we introduce the model and discuss its capabilities. In Section 3, we apply the model to conduct a parametric study of the alloy phase diagrams and find the conditions under which a stable polycrystalline state appears as a domain on a phase diagram. We study the structural and dynamic properties of the fully stabilized polycrystals and demonstrate the significant role of TJs in their stabilization. In Section 4, we summarize our findings and put them in perspective with the general problem of nano-stabilization.

2. Model formulation

We consider a simple square lattice forming a rectangular simulation block with periodic boundary conditions. The block contains N sites enumerated by the index $k = 1, 2, \dots, N$. Each site is interpreted as a small crystallite capable of adopting one of q distinct lattice orientations labeled by index $\sigma = 1, 2, \dots, q$.

For any given distribution of the orientations among the sites, each site k is characterized by the number n_k of nearest-neighbor sites whose orientations are different from σ_k . Thus,

$$n_k = \sum_{(kl)} \left(1 - \delta_{\sigma_k \sigma_l} \right), \quad (1)$$

where $\delta_{\sigma_k \sigma_l}$ is the Kronecker delta-function equal to 1 if $\sigma_k = \sigma_l$ and 0 otherwise. The symbol (kl) indicates summation over all neighbors l of site k . If all neighbors have the same orientation as the site k , then $n_k = 0$. If all neighbors have orientations different from σ_k , then $n_k = 4$.

Under certain conditions discussed later, the system breaks into domains composed of sites with the same orientation, which we interpret as grains separated by GBs. An example of a polycrystalline structure is shown in Fig. 1(a). In this and other figures in this paper, the colors represent different crystal orientations corresponding to different σ -numbers. Inside the grains, most sites have $n_k = 0$ (perfect lattice) and occasionally $n_k = 4$ (isolated inclusion with a “wrong” orientation) or $n_k = 1$ (neighbors of the isolated inclusion). In contrast, most sites in GB regions have $n_k = 2 \pm 1$. To identify GBs and track their motion, we introduce the GB locator function

$$\phi(n_k) = 1 - \frac{1}{4} (n_k - 2)^2, \quad (2)$$

which reaches the maximum value of 1 at sites with $n_k = 2$. Fig. 1(b) depicts a zoom-in portion of a polycrystalline structure with GBs revealed as sites with large $\phi(n_k)$ values. The image illustrates the effectiveness of the automated GB detection based on the function $\phi(n_k)$.

Next, we postulate that pairs of nearest-neighbor sites interact with a positive energy $J_{gg} > 0$ (repulsion) if their orientations are different and do not interact if the orientations are equal. The repulsive interactions drive the system into a polycrystalline state with relatively narrow GBs. The crystallographic energy of the system caused by such interactions is

$$E_{\text{cryst}} = \sum_k J_{gg} n_k \quad (3)$$

with $E_{\text{cryst}} = 0$ in the perfect single-crystalline state.

To describe solute thermodynamics, we use a lattice gas model with nearest-neighbor interactions. The solute atoms are distributed over the sites with a single atom per site. Each distribution is characterized by a set of occupation numbers ξ_k with $\xi_k = 1$ if the site k is occupied by a solute atom and $\xi_k = 0$ otherwise. The average solute concentration in the system is $c = \sum_k \xi_k / N$. We further assume that GBs create a potential field attracting the solute atoms. This field is represented by the following term in the total energy:

$$E_{sg} = \sum_k \xi_k J_s + \sum_k \xi_k J_{sg} \phi(n_k), \quad (4)$$

¹ More precisely, the free energy F is minimized with respect to the fraction f of GB sites: $dF/df = 0$. It is assumed that all GBs have the same width δ and uniform properties. Assuming also that $f \propto \delta/D$, where $D > 0$ is the average grain size, the stability condition becomes $dF/dD = 0$.

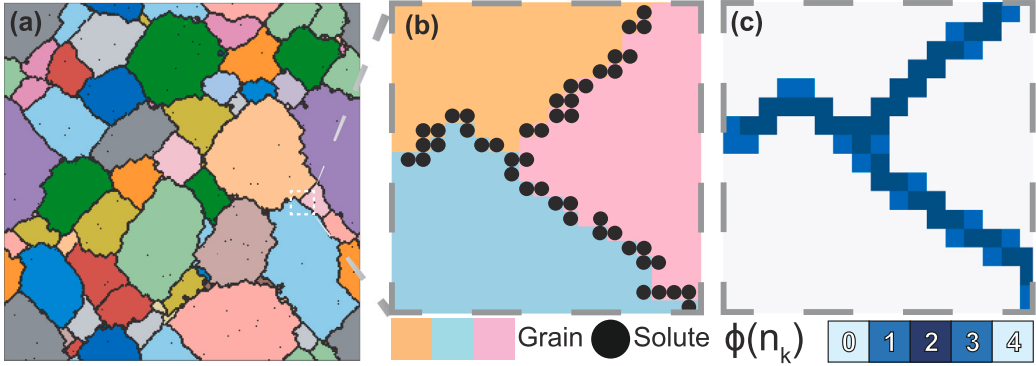


Fig. 1. (a) Snapshot of 256×256 polycrystalline system at temperature $T = 0.15$ and solute concentration $c = 0.1$. (b) Zoom-in view of a typical triple junction region with GBs colored according to the function $\phi(n_k)$. (c) The same zoom-in region as in (b) showing individual grains (colored regions) and solute atoms (black circles). (For interpretation of the references to color in this figure legend, the reader is referred to the web version of this article.)

where J_s has the meaning of the solute energy inside the grains. The product $\xi_k \phi(n_k)$ identifies GB sites occupied by a solute atom and shifts their energy by the amount $J_{sg} < 0$, creating a driving force for GB segregation. The parameter J_{sg} controls the strength of GB segregation (Fig. 1(c)) and is referred to as the segregation energy.

To account for solute–solute interactions, we add the following terms to the total energy:

$$E_{ss} = \frac{1}{2} \sum_k \sum_{(kl)} \xi_k \xi_l J_{ss} + \frac{1}{2} \sum_k \sum_{(kl)} \xi_k \xi_l J_{ssg} \phi(n_{k,l}). \quad (5)$$

Here, the products $\xi_k \xi_l$ locate pairs of nearest-neighbor atoms and the factor of $1/2$ eliminates their double-count. If both atoms are located inside a grain, their interaction energy is J_{ss} . If they are located in a GB region, the interaction energy is additionally shifted by the amount $J_{ssg} \phi(n_{k,l})$, where the GB locator $\phi(n_{k,l})$ depends on the average number of misoriented neighbors:

$$n_{k,l} = \frac{n_k + n_l}{2}. \quad (6)$$

Note that the two terms in Eq. (5) enable us to control of the solute–solute interactions inside the grains and in GB segregation atmospheres separately.

Putting all pieces together, the system energy E_i in each microstate $i = \{\sigma_k, \xi_k\}$ is the sum of three contributions:

$$E_i = E_{\text{cryst}} + E_{sg} + E_{ss}, \quad (7)$$

where the crystallographic energy E_{cryst} , the solute–GB interaction energy E_{sg} , and the solute–solute interaction energy E_{ss} are given by Eqs. (3), (4), and (5), respectively. The total energy depends on five physical parameters: J_{gg} , J_s , J_{sg} , J_{ss} , and J_{ssg} .

To evolve the system in time, we implement KMC simulations, in which the system transitions between microstates by overcoming energy barriers by thermal fluctuations. We adopt the harmonic transition state theory [57], in which the transition rate v_{ij} from microstate i to microstate j is given by

$$v_{ij} = v_0 \exp\left(-\frac{\epsilon_{ij}}{k_B T}\right), \quad (8)$$

where ϵ_{ij} is the transition barrier, k_B is Boltzmann's constant, and v_0 is the attempt frequency. The transition barrier ϵ_{ij} depends on the energy difference, $E_{ij} = E_j - E_i$, between the states. We adopt the nonlinear energy-barrier relation [32,33,55]:

$$\epsilon_{ij} = \begin{cases} \epsilon_0 \exp\left(\frac{E_{ij}}{2\epsilon_0}\right), & E_{ij} \leq 0, \\ E_{ij} + \epsilon_0 \exp\left(-\frac{E_{ij}}{2\epsilon_0}\right), & E_{ij} > 0 \end{cases} \quad (9)$$

where ϵ_0 is the unbiased energy barrier (when $E_j = E_i$). This relation ensures that transitions to higher (lower) energy microstates have a

higher (lower) barrier. If the destination microstate has a much lower energy than the current microstate, the transition barrier is exponentially small but never becomes zero. In other words, a strong driving force can suppress the transition barrier but never makes it exactly zero.

We consider two types of transitions, which we call flips and jumps. In a flip transition, a chosen site k switches its current orientation to one of the remaining $q - 1$ orientations with $\sigma_l \neq \sigma_k$. If a group of sites flips into the same orientation on one side of a GB, this can cause GB migration. In a jump event, a chosen solute atom jumps to a nearest-neighbor site if the latter is unoccupied. Such jumps represent solute diffusion. The flip and jump transitions are assigned unbiased barriers ϵ_0^g and ϵ_0^s , respectively. The flip barrier ϵ_0^g is the same for all sites and is related to the activation energy of GB migration. The jump barrier ϵ_0^s represents the activation energy of solute diffusion. In the present model, ϵ_0^s is assigned different values in GBs and inside the grains. Specifically, the unbiased barrier of a jump is

$$\epsilon_0^s = \epsilon_{00}^s [1 - \eta \phi(n_{k,l})], \quad (10)$$

where ϵ_{00}^s is the jump barrier inside the grains and $n_{k,l}$ is the average number of misoriented neighbors in the initial (k) and final (l) positions of the solute atom. The term in square brackets in Eq. (10) lowers the barrier for jumps within GB regions. Since in GB environments $\phi(n_{k,l}) \approx 1$, the barrier becomes approximately $\epsilon_0^s \approx \epsilon_{00}^s [1 - \eta]$. The parameter $0 \leq \eta < 1$ controls the decrease in the diffusion barrier leading to accelerated GB diffusion (“short-circuit” diffusion [58,59]) relative to the perfect lattice. In the simulations, we usually take $\eta = 1/2$ to match the experimentally established correlation $\epsilon_0^s \approx \epsilon_{00}^s/2$ between the activation energies of GB and lattice diffusion [58]. Note that a solute jump is generally accompanied by a change in the total energy ($E_{ij} \neq 0$). As a result, the actual jump barrier ϵ_{ij} is biased relative to ϵ_0^s according to Eq. (9).

In the KMC simulations, the number of solute atoms in the system is kept fixed while changes in the site orientations are unconstrained. Thus, the statistical ensemble is canonical for the solute atoms and grand-canonical with zero chemical potential for the site orientations. A rejection-free (n -way [60]) KMC algorithm is implemented. Technical details of this algorithm were presented in our previous publication [55]. In short, at each step, we apply Eqs. (8) and (9) to compute the rates of all possible flips at all sites and all possible jumps of all solute atoms. Normalization of these rates gives us the transition probabilities to all microstates j accessible from the given microstate i . A random number then selects a new microstate in proportion to its transition probability. The clock is advanced according to the total escape rate from the microstate i , and the process repeats from the new microstate.

Two features distinguish our KMC algorithm from previous Monte Carlo simulations using the Ising and Potts models with solutes [6,11, 61–64]. Firstly, we replace the Metropolis scheme with the probability

calculations using the actual transition barriers. This scheme is more suitable for the modeling of solute diffusion and GB migration than the Metropolis algorithm. The latter correctly samples canonical fluctuations in equilibrium states but the path towards equilibrium is not guaranteed to be physically meaningful. Secondly, previous simulations within the Potts model only allowed flips to one of the neighboring orientations. In contrast, we allow the current orientation to switch to *any* of the alternative $q - 1$ orientations. This imposes fewer constraints on the system evolution and captures processes such as new grain nucleation and orientational fluctuations in single crystals as well as disordered, liquid-like structures.

The KMC simulations were performed in normalized variables whose relations to the physical variables are summarized [Table 1](#). All energies are normalized by J_{gg} , and the unit of time is v_0^{-1} . The attempt frequency v_0 is assumed to be the same for all transitions. From now on, we only use the normalized variables denoted by the same symbols as the respective physical variables. In most simulations reported below, we assume $J_s = 0$.

3. Results

3.1. The melting transition in the solute-free system

Before studying the alloy systems, we performed solute-free simulations to validate our methodology and software. [Fig. 2\(a\)](#) shows the computed orientational order parameter $\langle m \rangle$ as a function of temperature for three different q values. The order parameter was computed by [65]

$$\langle m \rangle = \left\langle \frac{(N_m/N)q - 1}{q - 1} \right\rangle, \quad (11)$$

where N_m is the number of sites with the dominant orientation and the angular brackets represent averaging over many KMC steps. Below a critical point, a system initiated with a single orientation remains predominantly in this orientation ($\langle m \rangle \approx 1$) except for a small concentration of misoriented sites and their small clusters ([Fig. 2\(b\)](#)). The local orientation flips are caused by thermal fluctuations and are revealed by our simulations because we allow flip transitions to all orientations without restricting them to nearest neighbors. Above the critical temperature T_c , the system becomes fully disordered ($\langle m \rangle \rightarrow 0$) with weak short-range dynamic correlations among the site orientations ([Fig. 2\(d\)](#)).

In the magnetic terminology, the states below and above T_c are ferromagnetic and paramagnetic, respectively. Since we interpret the indices σ_k as crystallographic orientations, we refer to the two states as a single crystal and liquid, respectively. Accordingly, the critical temperature is interpreted as the melting point, which in the 2D Potts model with $q > 4$ is a first-order phase transition [66,67]. Since the ensemble is grand canonical, only single-phase states are possible as equilibrium states. However, the simulations also capture transient two-phase states as the system evolves from one phase to the other. An example of a transient solid-liquid state is shown in [Fig. 2\(c\)](#). The relatively sharp interphase boundaries are consistent with the first-order nature of melting in this model.

The computed values of T_c closely follows the analytical solution of the Potts model for the simple square lattice [66,67]:

$$T_c = \frac{1}{\ln(1 + \sqrt{q})}.$$

As the number of orientations q increases, the melting temperature decreases ([Fig. 2\(a\)](#)), which is consistent with the increased configurational entropy of the liquid phase. Note that the discontinuity of the order parameter at the melting point sharply increases with q .

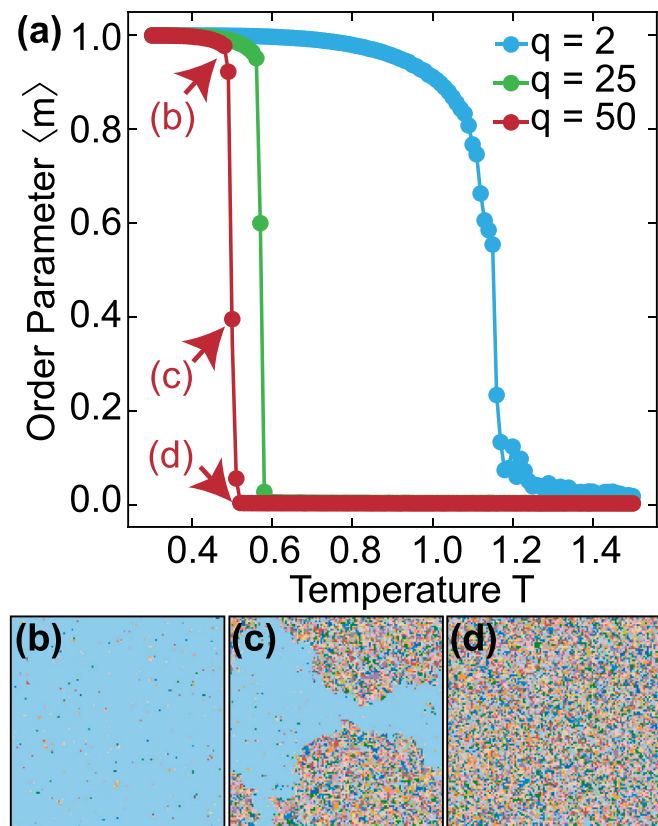


Fig. 2. (a) Phase diagram of solute-free Potts model computed on a 128×128 grid for three representative q -values. (b) Single crystalline state with occasional isolated inclusions below the critical point. (c) Transient two-phase state showing solid-liquid interphase boundaries. (d) Fully disordered (liquid-like) state above the critical point.

3.2. The alloy phase diagrams

In the presence of solute atoms, the phase diagrams become more complex. A parametric study was performed to explore representative regions of the large parameter space of the model. The results were presented in the form of temperature-composition phase diagrams showing the domains of single phases and phase coexistences. For each set of model parameters, a large number of simulations were performed on a grid of temperatures and solute concentrations between $c = 0$ to $c = 1$. For each temperature-composition pair, a 64×64 system was equilibrated by KMC simulations until all properties reached time-independent values. Large solute diffusivities were implemented to accelerate the convergence. Different initial states were tested to verify that the system always arrives at the same final state. Several structural and dynamic properties were computed to identify the phases automatically in addition to visual inspection. Since this construction has a discrete character, the lines delineating different domains on the phase diagrams are only accurate to within the temperature-composition grid size $\Delta T \times \Delta c$, which was typically 0.02×0.1 . Supplementary Figure 1 presents a typical phase diagram together with the grid used for its construction. Supplementary Figure 2 shows typical structures of all phases appearing on the phase diagrams alongside the convergence plots demonstrating that these structures do not depend on the initial state of the KMC simulations.

We first discuss the simplest case when the solute atoms are attracted to GBs ($J_{sg} = -1.6$) to form segregation atmospheres but do not interact with each other ($J_{ss} = J_{sgs} = 0$). Formally, the solute atoms form a perfect solution. In reality, they still interact with each

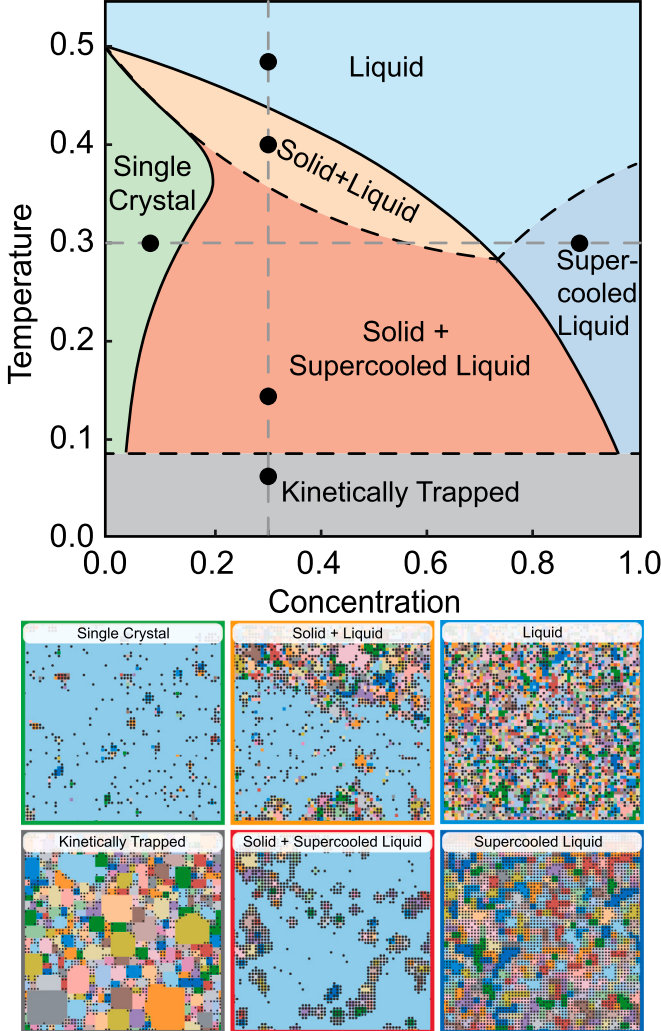


Fig. 3. Phase diagram when the solute atoms are attracted to GBs ($J_{sg} = -1.6$) but do not interact with each other ($J_{ss} = J_{sg} = 0$). The images show the structures corresponding to the black circles on the diagram. The site orientations are color-coded and the solute atoms are represented by black dots. (For interpretation of the references to color in this figure legend, the reader is referred to the web version of this article.)

other indirectly through coupling to the orientational order parameter. Indeed, although the solute atoms are primarily attracted to GBs, which are identified using the GB locator function $\phi(n_k)$, isolated misoriented sites and their small clusters can also act as attractors because they have nonzero $\phi(n_k)$ values. Occasionally, the solute atoms confuse such misoriented inclusions with GBs and are attracted to them. For example, if a site inside a single-crystalline region flips into a “wrong” orientation, it can attract two solute atoms, which will then try to remain neighbors of that site. The imposed positional correlations between pairs of solute atoms acts as an effective attractive interaction. In most cases, such interactions are overshadowed by the strong attraction to GBs. However, they can still affect the shape of the phase diagram. There is also a reciprocal effect, in which the solute atoms promote orientational disorder among their neighbors due to their attraction to misoriented sites. In particular, the solute atoms are attracted to liquid environments and stabilize the liquid phase.

The phase diagram in Fig. 3 features a single-crystalline phase, a liquid solution phase, and a solid–liquid coexistence domain between the solidus and liquidus lines. The negative slope of the liquidus line is consistent with the solute-induced liquid stabilization mentioned

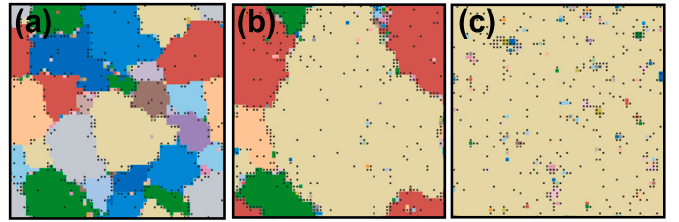


Fig. 4. Snapshots of KMC simulations of an isolated grain within the single-crystalline domain on the phase diagram in Fig. 3 ($c = 0.1$, $T = 0.36$). (a) Initial state. (b) Intermediate state showing grain coarsening and beginning of abnormal grain growth. (c) Final single-crystalline state.

above. The images next to the phase diagram display typical alloy structures with color-coded crystallographic orientations and the solute atom distributions shown by black dots. The bottom part of the diagram represents kinetically trapped states that could not be fully equilibrated on the time scale of our simulations.

According to the diagram in Fig. 3, the ground state of the solid solution is a single crystal. A polycrystalline state is unstable and must transform into a single crystal. To verify this prediction, we chose a classical polycrystalline structure as the initial state of KMC simulations (Fig. 4(a)). The temperature and composition were selected within the single-crystalline domain on the phase diagram. During the simulation, the structure was found to coarsen by first normal and later abnormal grain growth (Fig. 4(b)), and eventually transformed into a single crystal (Fig. 4(c)). This behavior is typical for unstable polycrystals with $\gamma > 0$.

We find that the liquid structure undergoes marked changes with decreasing temperature and increasing solute concentration. At high temperatures and low-to-moderate solute concentrations, the liquid solution is similar to the solute-free liquid (compare Figs. 2(d) and 3). The orientations σ_k randomly fluctuate from one site to the next with little correlation. Sites with $n_k \geq 3$ dominate. When more solute is added and/or the temperature is decreased, the liquid develops a more coarse-grained structure with stronger spatial correlations between neighboring orientations. The sites with $n_k \leq 2$ become prevalent. This structure can be described as a collection of orientational domains a few inter-site spacings in size, which constantly appear and disappear. We call this form of liquid a “supercooled liquid”. Several structural characteristics were computed to quantify the difference between the two liquids. For example, Supplementary Figure 3 shows a set of histograms of n_k values in the $c = 1$ alloy. The histograms were obtained by averaging over long KMC runs after the system reached equilibrium. As temperature decreases, the histograms shift towards smaller n_k values and reverse their skewness from right to left. These trends are quantified in Fig. 5(a, b), showing the average number of unlike neighbors \bar{n}_k and the skewness parameter as functions of temperature. The plots show that \bar{n}_k changes its behavior and the skewness reverses its sign at $T \approx 0.35$.

In addition to the structural distinctions, the supercooled liquid displays much slower dynamics compared to the high-temperature liquid. For example, Fig. 5(c) shows the Arrhenius plot of the orientation switching rate r as a function of temperature at a fixed chemical composition. To calculate r , we keep track of the orientation changes at all sites during an equilibrium KMC run. At each site, we compute the time interval Δt between the moment when the site switched to its current orientation and the moment when it switches to a new orientation. After the switch, we reset the clock and start counting the time to the next switch, and so on. The value $\bar{\Delta t}$ averaged over a long KMC run and all sites represents the time scale on which the sites preserve their orientation. Accordingly, $r = 1/\bar{\Delta t}$ characterizes the rate of orientational changes in the liquid, which is a measure of its intrinsic dynamics. The plot of $\log r$ versus $1/T$ shown in Fig. 5(c) displays a

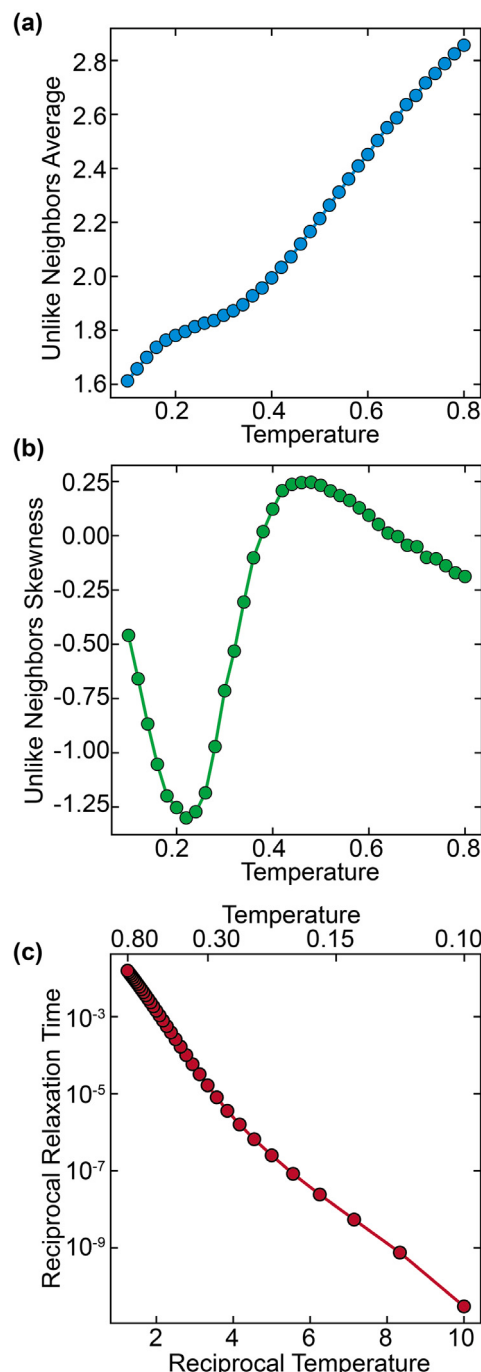


Fig. 5. Structural and kinetic characteristics of the pure solvent liquid ($c = 1$) as a function of temperature. The model parameters are $J_{sg} = -1.6$, $J_{ss} = J_{ssg} = 0$. (a) The average number of unlike neighbors \bar{n}_k . (b) The skewness of n_k histograms. (c) Arrhenius diagram of the orientation switching rate r .

non-Arrhenius behavior. The increase in r with temperature accelerates above $T \approx 0.35$, which is approximately where the structural changes in the liquid are observed. We associate the structural and dynamical changes in the liquid at $T \approx 0.35$ with the formation of supercooled liquid. The temperature of this transition depends on the chemical composition. Because this transition is continuous, its position on the phase diagram is approximate and is shown by a dashed line. This line separates the stable polycrystalline state from a single crystal with inclusions assuming a threshold grain size of 12 sites.

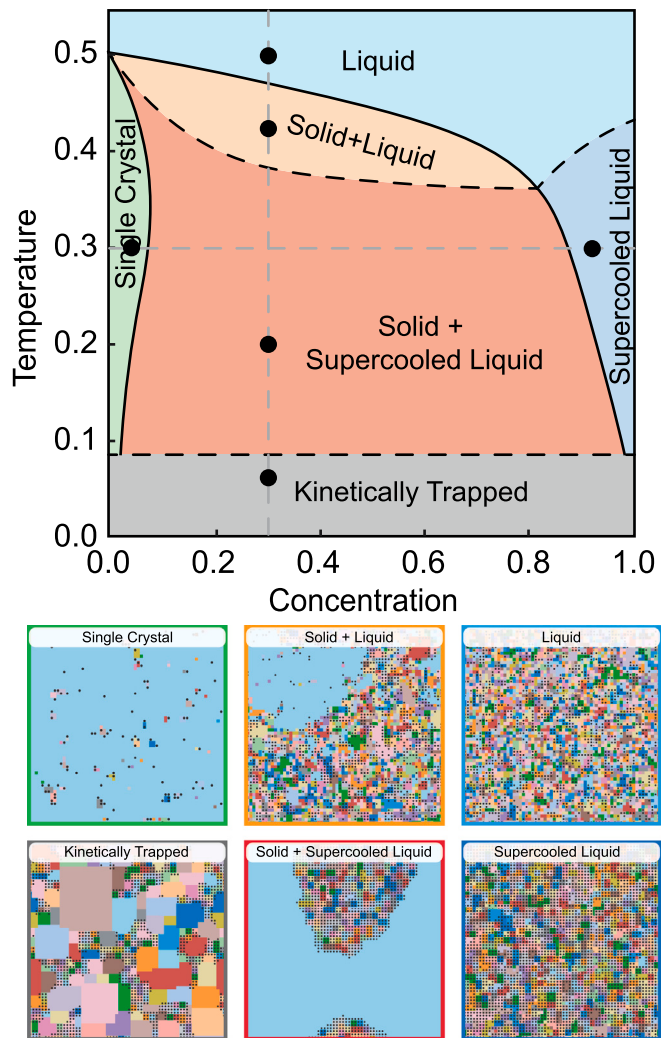


Fig. 6. Phase diagram when the solute atoms are attracted to GBs ($J_{sg} = -1.6$) and interact by attractive forces ($J_{ss} = -0.25$, $J_{ssg} = -0.05$). The images show the structures corresponding to the black circles on the diagram. The site orientations are color-coded and the solute atoms are represented by black dots. (For interpretation of the references to color in this figure legend, the reader is referred to the web version of this article.)

Next, we keep the same segregation energy ($J_{sg} = -1.6$) but turn on the solute–solute interactions making them attractive. For example, we set $J_{ss} = -0.25$ in the grains and $J_{ssg} = -0.05$ at GBs. The phase diagram (Fig. 6) is qualitatively similar to the previous one, except that the solid solubility is markedly smaller and the liquidus line is shifted towards higher temperatures, opening a wider miscibility gap. It becomes especially clear that the supercooling transition in the liquid changes the solid–liquid interphase boundaries in two-phase alloys. While at high temperatures such boundaries are rather fluffy, below the supercooling transition they become remarkably sharp.

The most interesting case arises when the segregation energy remains the same as above ($J_{sg} = -1.6$) but the solute–solute interactions become repulsive (e.g., $J_{ss} = 0.25$ in the grains and $J_{ssg} = 0.05$ at GBs). The phase diagram changes substantially (Fig. 7). The solidus line shifts towards larger solute concentrations, narrowing the miscibility gap. Most importantly, two different solid–solution structures can now exist under the solidus line: the previously observed single-crystalline phase and a new stable polycrystalline phase. The transition between the single-crystalline and polycrystalline structures is continuous and is marked on the phase diagram with a dashed line.

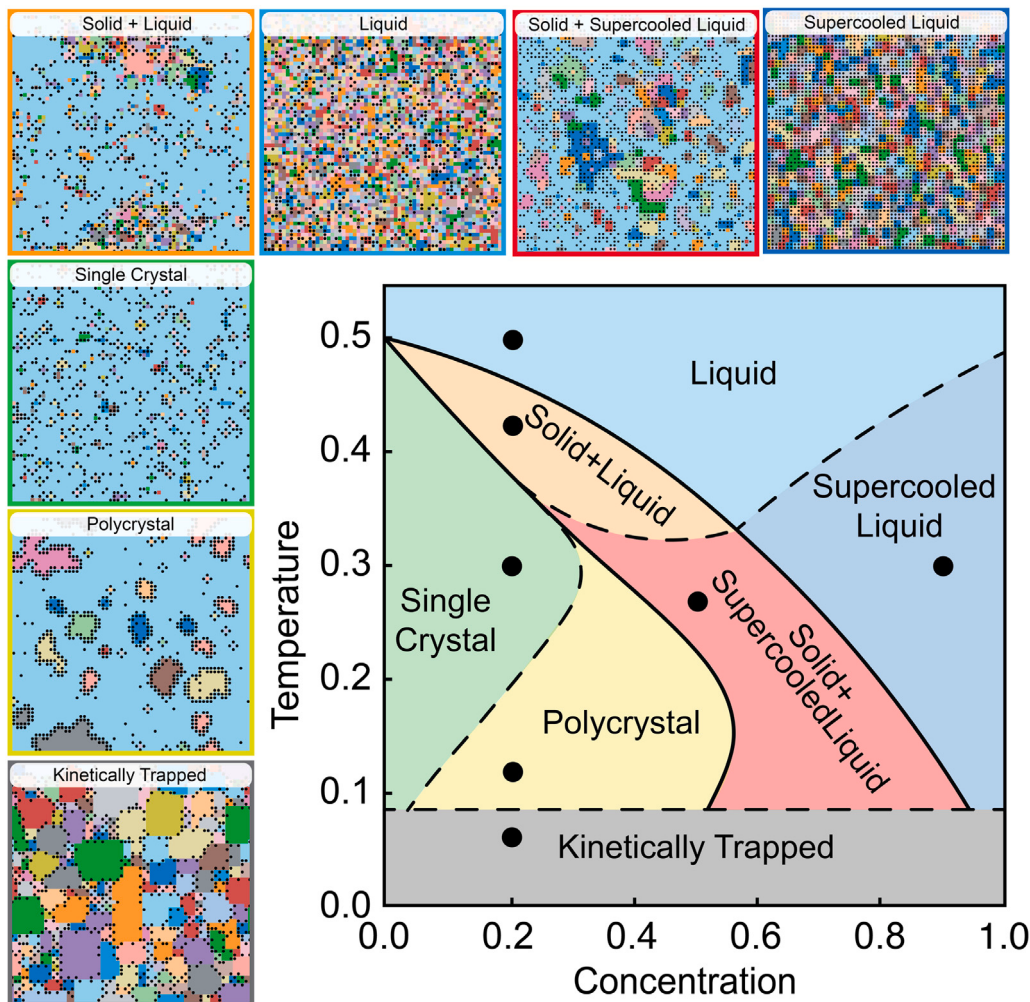


Fig. 7. Phase diagram when the solute atoms are attracted to GBs ($J_{sg} = -1.6$) and interact by repulsive forces ($J_{ss} = 0.25$, $J_{sg} = 0.05$). The images show the structures corresponding to the black circles on the diagram. The site orientations are color-coded and the solute atoms are represented by black dots. (For interpretation of the references to color in this figure legend, the reader is referred to the web version of this article.)

3.3. The stable polycrystalline state

In this section, we examine the stable polycrystalline structure in more detail. The equilibrium nature of this structure was confirmed by restarting KMC simulations from different initial states and verifying that we always arrive at the same polycrystalline structure. One of the convergence tests is demonstrated in Fig. 8. KMC simulations were performed at the temperature of $T = 0.1$ and the chemical composition of $c = 0.2$. This state falls into the polycrystalline field on the phase diagram (Fig. 7). In simulations starting from a single crystal with a random solute distribution, the solute atoms create a set of small misoriented clusters, which then grow and eventually form a set of isolated grains embedded in the matrix of the initial grain. In the final state, most of the solute atoms are located at the boundaries of the embedded grains. The grain size fluctuates around a time-independent average value. Alternatively, simulations were started from a random distribution of the solute atoms and orientations over the sites. This initial structure is similar to the high-temperature liquid solution. First, randomly oriented crystalline grains nucleate at multiple locations, grow, and eventually impinge on each other to form a classical polycrystalline structure with strong solute segregation. This structure is unstable and coarsens with time following the classical grain-growth scenario. At some point, the grain growth becomes abnormal, with one grain starting to consume all other grains. However, in contrast to the classical behavior, a set of isolated grains remains embedded in the

growing grain, until the latter spreads over the entire simulation box and becomes a matrix grain. The final state of this evolution is the same as when starting from the single-crystalline state. The Supplementary Figure 2 shows that the system energy converges to the same value in both cases. These and similar tests confirm that the polycrystalline structure found here is indeed the thermodynamic ground state of the alloy.

We emphasize that the equilibrium polycrystalline structure is not static. The grains are not frozen in a special configuration that minimizes the free energy. Instead, this is a state of *dynamic equilibrium*, in which some grains grow while other grains shrink. For instance, Fig. 9(a) displays a set of snapshots of an equilibrated polycrystal taken at different moments of time. While all structures look similar, the positions, sizes, and shapes of individual grains change from one snapshot to another. It is only the *average* structural properties of the polycrystal that remain constant. Figs. 9(c, d) demonstrate that, once equilibrium is reached, all structural and dynamic characteristics of the polycrystal fluctuate around constant values. Such characteristics include the average number of atoms in a grain (Fig. 9(c)) and the total number of grains in the system (Fig. 9(d)), which display significant variations around constant average values. In Fig. 9(b), we plot the sizes of ten selected grains as functions of time. The plot tells us a story of the birth, life and death of the grains. Some new grains appear (e.g., by splitting from a larger grain or by homogeneous nucleation),

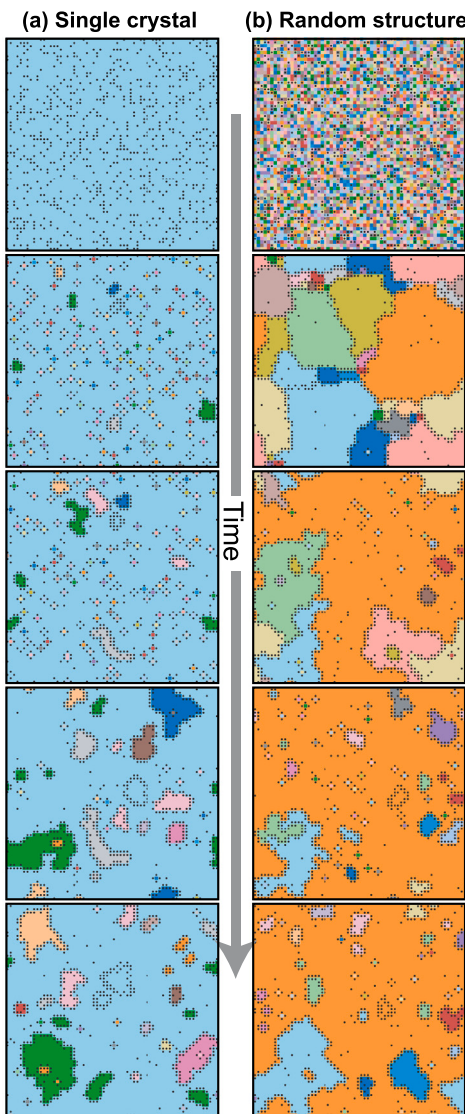


Fig. 8. Structure evolution (left to right) of the alloy with the composition $c = 0.2$ at temperature $T = 0.1$ starting from (a) single crystal and (b) randomly distributed site orientations. The model parameters are the same as for the phase diagram in Fig. 7. In both cases, the system converges to the stable polycrystal.

grow in size, then shrink, and some eventually disappear. Some of the nearly extinct grains start growing again.

Another prominent feature of the stable polycrystals is the absence of TJs. To eliminate them, the grains form isolated inclusions within a matrix grain. Occasionally, nested structures are observed, with a smaller grain enclosed within a larger. As the grains grow and shrink, they always stay clear of each other and avoid even touching. This TJ avoidance suggests a positive TJ free energy. Fig. 10(a) illustrates the TJ avoidance effect. In an alloy known to be a stable polycrystal in thermodynamic equilibrium, two grains separated by a planar GB have been artificially embedded in a matrix grain. This structure contains two triple junctions. During the KMC simulations, the grains develop extensive protrusions, which later split off as smaller grains. Eventually, the initial grains fully separate from each other, eliminating the TJs. When the same initial state is created in an alloy whose ground state is a single crystal, the scenario is different (Fig. 10(b)). Both grains shrink and eventually disappear while maintaining contact and thus the two TJs.

4. Discussion and conclusions

We proposed a simple 2D model of a polycrystalline alloy combining the Potts model for grain orientations with a lattice-gas model for solute thermodynamics and diffusion. The model couples the evolution of the crystal orientations (and thus GB migration) to thermodynamic properties of the alloy and the solute diffusion. It recognizes that the thermodynamic parameters and the solute diffusion coefficients are generally different inside the grains and at GBs. The model goes beyond the uniform boundary approximation, automatically includes nucleation processes due to its stochastic nature, and captures the diffusive time scales not accessible by material-specific methods such as molecular dynamics simulations. The model is solved by KMC simulation with nonlinear transition barriers. We have applied this model to investigate the problem of polycrystalline stability, but it has a much broader applicability. It can be used to study other processes, such as solute drag and the impact of solute segregation on GB diffusion.

The main outcome of this work is the confirmation that a polycrystalline alloy can be thermodynamically stable. The initial prediction of full stabilization [46,47] and the subsequent thermodynamic analyses [48–53,55] were based on strong assumptions. For example, they disregarded the role of TJs and assumed that all GBs were equal. The present model is free from those assumptions and nevertheless confirms that the fully stabilized polycrystalline state exists and is consistent with thermodynamics.

The KMC simulations within this model helped us realize that the minimum of the total free energy cannot be achieved by designing a particular polycrystalline structure with special grain shapes satisfying the equilibrium conditions among all capillarity vectors at all TJs. Such a structure is unlikely to exist. Instead, the structure minimizing the total free energy is in a state of dynamic equilibrium between the competing processes of grain growth and grain refinement.

Thermodynamic analyses within the uniform boundary model [46–53,55] predict that the total free energy minimum requires that the GB free energy be zero. The real GBs are not equal, and the $\gamma = 0$ condition is unlikely to be achieved in all of them simultaneously. Our simulations suggest that the $\gamma = 0$ condition should be met in an average sense, with GBs alternating between positive and negative γ values and the polycrystalline structure “breathing” by constantly switching between the grain coarsening and grain refinement.

TJs play a prominent role in the stabilization problem. In thermodynamically unstable polycrystals, their total free energy is smaller than the total GB free energy, making the latter the leading driving force for the grain coarsening. However, when the GB free energy tends to zero, or simply becomes small enough, the elimination of TJs becomes the leading driver of the structural evolution. For full stabilization, their free energy (per unit length) might also be suppressed to zero by an appropriate solute segregation. However, it seems highly improbable that this can be achieved at all TJs simultaneously with the $\gamma = 0$ condition at all GBs. Most likely, the structure will try to eliminate the TJ, and the quadruple points with them. This can be achieved by creating a set of embedded grains within a large matrix grain, which is exactly the type of structure we see in the simulations.

An important aspect not discussed in this paper is the role solute diffusion. The latter must be fast enough to ensure that the solute atoms can catch up with the moving GBs and keep their free energy close to zero. The role of solute diffusion was preliminary explored in our previous publication [55] but should be investigated more systematically in the future.

Although the proposed model does not represent any particular material and is intended for a generic analysis of thermodynamics and kinetics of polycrystalline alloys, it was important to map the domain of the model parameters explored in our simulations onto thermodynamic properties of real alloy systems. In the Supplementary Information file accompanying this article, we have expressed the model parameters through the experimentally accessible properties such as the heat of

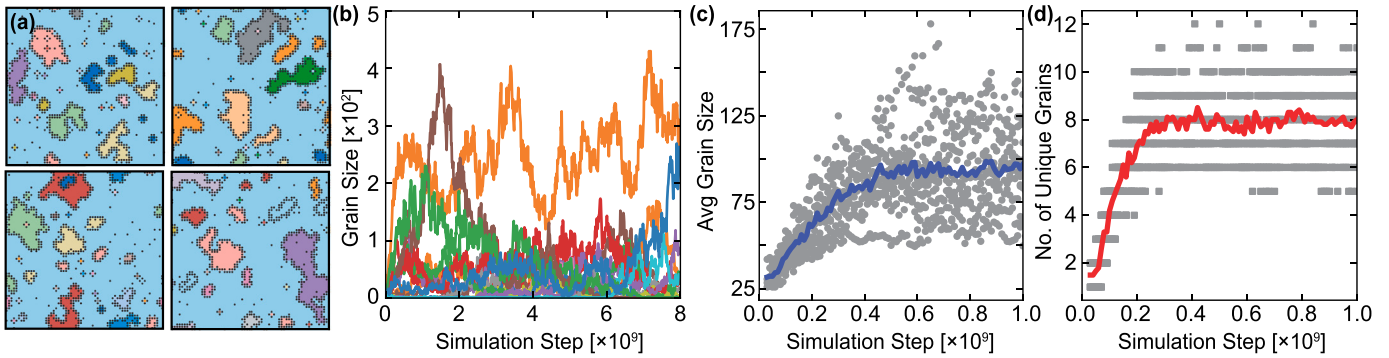


Fig. 9. (a) Snapshots of equilibrium configurations during KMC simulations of a stable polycrystalline alloy. (b) Grain size evolutions for ten selected grains, showing their shrinkage and growth. (c) The sizes of individual grains in ten KMC runs as a function of time. The blue curve represents the average grain size. (d) The number of unique grains as a function of time in ten KMC runs. The red curve represents the average number of grains. The model parameters are $J_{sg} = -1.6$, $J_{ss} = 0.25$, $J_{ssg} = 0.05$. (For interpretation of the references to color in this figure legend, the reader is referred to the web version of this article.)

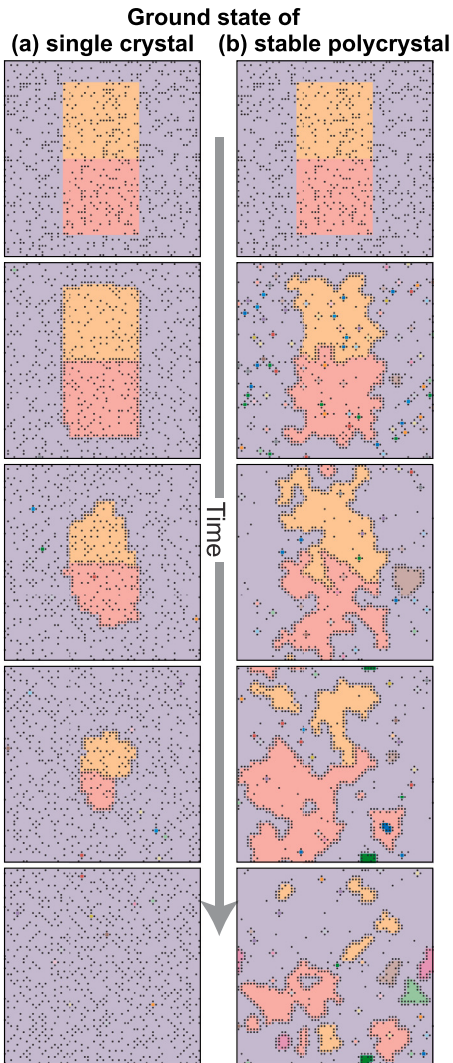


Fig. 10. Time evolution (left to right) of two grains initially in contact with each other and forming two TJs. The model parameters are $J_{sg} = -1.6$, $J_{ss} = 0.25$, $J_{ssg} = 0.05$. (a) The alloy at $T = 0.1$ and $c = 0.2$ when the ground state is a stable polycrystal. (b) The alloys at $T = 0.1$ and $c = 0.2$ when the ground state is a single crystal.

Table 1
Table of physical and normalized variables in this model.

Variable	Physical	Normalized
Temperature	T	$k_B T / J_{gg}$
Total energy	E	E / J_{gg}
Solute-interface interaction energy	J_{sg}	J_{sg} / J_{gg}
Solute interaction energy in grains	J_{ss}	J_{ss} / J_{gg}
Additional solute interaction energy in GBs	J_{ssg}	J_{ssg} / J_{gg}
Time	t	$t v_0$
GB energy	γ	$\gamma A / J_{gg}$

Table 2

Potts model parameters normalized to J_{gg} are compared with thermodynamic properties: grain boundary segregation energy E_s , regular solution parameters inside the grains (Ω) and in grain boundaries (Ω'), and dilute heat of mixing (H_{mix}). The cases 1, 2, and 3 correspond to parameter sets used for computing the phase diagrams shown in Figs. 3, 6, and 7 of the main text.

Parameters	Case 1	Case 2	Case 3
J_{sg} / J_{gg}	-1.6	-1.6	-1.6
J_{ss} / J_{gg}	0	-0.25	0.25
J_{ssg} / J_{gg}	0	-0.05	0.05
E_s (kJ/mol)	-136	-136	-136
Ω (kJ/mol)	0	10.61	-10.61
Ω' (kJ/mol)	0	12.73	-12.73
H_{mix} (kJ/mol)	0	50.94	-50.94

solution in the dilute limit, H_{mix} , the GB segregation energy E_s , the GB free energy in the pure solvent material γ , and the regular solution parameter Ω' inside the GBs (which is generally different from Ω within the grains). The estimates are based on two reasonable assumptions: the area per atom in the GB core is on the order of 1 nm^2 , and γ is about 1 J/m^2 .

Table 2 summarizes the results for three representative parameter sets corresponding to the phase diagrams shown in Figs. 3, 6, and 7. The predicted magnitudes of E_s , Ω , Ω' , and H_{mix} are well within the typical ranges reported in previous publications [5–9,11,68]. A notable feature of the present simulations is that the stable polycrystalline structure was found in alloys with a negative heat of mixing, corresponding to the ordering trend (Table 2 and Fig. 7). Most of the previous calculations [5–9,11,68] considered phase-separating alloys with $H_{mix} > 0$. However, recent publications [7,68] extended the previous analyses to alloys with $H_{mix} < 0$ and still reported stable nanocrystalline states. For example, Figure 6 in [68] presents a diagram showing a nanocrystalline stability domain at $\Omega' < \Omega < 0$. Furthermore, the values of Ω and Ω' for the representative point g in this domain are comparable to the respective values in Table 2. A more detailed quantitative comparison with previous publications [5–9,11,68] is complicated due to intrinsic differences between models (see Supplementary Information

for more detail), but the qualitative agreement indicates that the model parameters investigated in this paper are practically relevant.

Due to the 2D constraint and the generic character of this model, the results do not allow us to pinpoint a particular alloy system in which a nano-stabilization can be achieved. However, we believe that the results can be useful as a general guide in this pursuit. In particular, they provide a glimpse into what a fully stabilized NC state would look like if it were achieved experimentally in the future.

CRediT authorship contribution statement

Omar Hussein: Writing – original draft, Visualization, Validation, Software, Methodology, Investigation, Formal analysis. **Yuri Mishin:** Writing – review & editing, Supervision, Project administration, Funding acquisition, Conceptualization.

Declaration of competing interest

The authors declare that they have no known competing financial interests or personal relationships that could have appeared to influence the work reported in this paper.

Acknowledgments

This research was supported by the National Science Foundation, Division of Materials Research, under Award no. DMR-2103431.

Appendix A. Supplementary data

Supplementary material related to this article can be found online at <https://doi.org/10.1016/j.actamat.2025.121545>.

References

- [1] M.A. Meyers, A. Mishra, D.J. Benson, Mechanical properties of nanocrystalline materials, *Prog. Mater. Sci.* 51 (2006) 427–556.
- [2] K.A. Darling, Y. Mishin, N.N. Thadhani, Q. Wei, K. Solanki, Mechanical behavior of microstructurally stable nanocrystalline alloys: Processing, properties, performance, and prospects, *Prog. Mater. Sci.* 155 (2026) 101519.
- [3] J.W. Gibbs, *The Collected Works of J. W. Gibbs*, Vol. 1, Yale University Press, New Haven, 1948.
- [4] A.J. Detor, C.A. Schuh, Grain boundary segregation, chemical ordering and stability of nanocrystalline alloys: Atomistic computer simulations in the Ni-W system, *Acta Mater.* 55 (2007) 4221–4232.
- [5] T. Chookajorn, H.A. Murdoch, C.A. Schuh, Design of stable nano-crystalline alloys, *Science* 337 (2012) 951–953.
- [6] T. Chookajorn, C.A. Schuh, Thermodynamics of stable nanocrystalline alloys: A Monte Carlo analysis, *Phys. Rev. B* 89 (2014) 064102.
- [7] A.R. Kalidindi, C.A. Schuh, Stability criteria for nanocrystalline alloys, *Acta Mater.* 132 (2017) 128–137.
- [8] T.C.A.R. Kalidindi, C.A. Schuh, Nanocrystalline materials at equilibrium: A thermodynamic review, *JOM* 67 (2015) 2834–2843.
- [9] A.R. Kalidindi, C.A. Schuh, Stability criteria for nanocrystalline alloys, *J. Mater. Res.* 32 (2017) 1093–2002.
- [10] H.A. Murdoch, C.A. Schuh, Stability of binary nanocrystalline alloys against grain growth and phase separation, *Acta Mater.* 61 (2013) 2121–2132.
- [11] J.R. Trelewicz, C.A. Schuh, Grain boundary segregation and thermodynamically stable binary nanocrystalline alloys, *Phys. Rev. B* 79 (2009) 094112.
- [12] A.E. Perrin, C.A. Schuh, Stabilized nanocrystalline alloys: The intersection of grain boundary segregation with processing science, *Annu. Rev. Mater. Res.* 51 (2021) 241–268.
- [13] C.C. Koch, R.O. Scattergood, K.A. Darling, J.E. Semones, Stabilization of nanocrystalline grain sizes by solute additions, *J. Mater. Sci.* 43 (2008) 7264–7272.
- [14] K.A. Darling, M.A. Tschoop, B.K. VanLeeuwen, M.A. Atwater, Z.K. Liu, Mitigating grain growth in binary nanocrystalline alloys through solute selection based on thermodynamic stability maps, *Comput. Mater. Sci.* 84 (2014) 255–266.
- [15] M. Saber, H. Kotan, C.C. Koch, R.O. Scattergood, Thermodynamic stabilization of nanocrystalline binary alloys, *J. Appl. Phys.* 113 (2013) 065515.
- [16] M. Saber, H. Kotan, C.C. Koch, R.O. Scattergood, A predictive model for thermodynamic stability of grain size in nanocrystalline ternary alloys, *J. Appl. Phys.* 114 (2013) 103510.
- [17] W. Xing, A.R. Kalidindi, D. Amram, C.A. Schuh, Solute interaction effects on grain boundary segregation in ternary alloys, *Acta Mater.* 161 (2018) 285–294.
- [18] N. Zhou, J. Luo, Developing thermodynamic stability diagrams for equilibrium-grain-size binary alloys, *Mater. Lett.* 115 (2014) 268–271.
- [19] F. Abdeljawad, S.M. Foiles, Stabilization of nanocrystalline alloys via grain boundary segregation: A diffuse interface model, *Acta Mater.* 101 (2015) 159–171.
- [20] F. Abdeljawad, P. Lu, N. Argibay, B.G. Clark, B.L. Boyce, S.M. Foiles, Grain boundary segregation in immiscible nanocrystalline alloys, *Acta Mater.* 126 (2017) 528–539.
- [21] M. Alkayyali, F. Abdeljawad, Grain boundary solute drag model in regular solution alloys, *Phys. Rev. Lett.* 127 (2021) 175503.
- [22] J.W. Cahn, The impurity-drag effect in grain boundary motion, *Acta Metall.* 10 (1962) 789–798.
- [23] N. Ma, S.A. Dregia, Y. Wang, Solute segregation transition and drag force on grain boundaries, *Acta Mater.* 51 (2003) 3687–3700.
- [24] I. Toda-Caraballo, C. Capdevila, G. Pimentel, C.G. De Andres, Drag effects on grain growth dynamics, *Comput. Mater. Sci.* 68 (2013) 95–106.
- [25] R. Koju, Y. Mishin, Direct atomistic modeling of solute drag by moving grain boundaries, *Acta Mater.* 198 (2020) 111–120.
- [26] M. Hillert, Solute drag, solute trapping and diffusional dissipation of Gibbs energy, *Acta Mater.* 47 (1999) 4481–4505.
- [27] M. Hillert, J. Odquist, J. Agren, Comparison between solute drag and dissipation of gibbs energy by diffusion, *Scr. Mater.* 45 (2001) 221–227.
- [28] Y. Mishin, Solute drag and dynamic phase transformations in moving grain boundaries, *Acta Mater.* 179 (2019) 383–395.
- [29] R.K. Koju, Y. Mishin, The role of grain boundary diffusion in the solute drag effect, *Nanomaterials* 11 (2021) 2348.
- [30] A. Suhane, D. Scheiber, M. Popov, V.I. Razumovskiy, L. Romaner, M. Militzer, Solute drag assessment of grain boundary migration in Au, *Acta Mater.* 224 (2022) 117473.
- [31] J. Svoboda, F.D. Fischer, M. Leindl, Transient solute drag in migrating grain boundaries, *Acta Mater.* 59 (2011) 6556–6562.
- [32] Y. Mishin, Stochastic model and kinetic monte carlo simulation of solute interactions with stationary and moving grain boundaries. i. model formulation and application to one-dimensional systems, *Phys. Rev. Mater.* 7 (2023) 063403.
- [33] Y. Mishin, Stochastic model and kinetic monte carlo simulation of solute interactions with stationary and moving grain boundaries. ii. application to two-dimensional systems, *Phys. Rev. Mater.* 7 (2023) 063404.
- [34] W.B. Li, K.E. Easterling, The influence of particle shape on Zener drag, *Acta Metall. Mater.* 38 (1990) 1045–1052.
- [35] R. Koju, K. Darling, L.J. Kecske, Y. Mishin, Zener pinning of grain boundaries and structural stability of immiscible alloys, *JOM* 68 (2016) 1596–1604.
- [36] P.A. Manohar, M. Ferry, T. Chandra, Five decades of the Zener equation, *ISIJ Int.* 38 (1998) 913–924.
- [37] M. Miodownik, E.A. Holm, G.N. Hassold, Highly parallel computer simulations of particle pinning: Zener vindicated, *Scr. Mater.* 42 (2000) 1173–1177.
- [38] E. Nes, N. Ryum, O. Hunderi, On the Zener drag, *Acta Metall.* 33 (1985) 11–22.
- [39] C.L. Di Prinzio, E. Druetta, O.B. Nasello, More about Zener drag studies with Monte Carlo simulations, *Modelling Simul. Mater. Sci. Eng.* 21 (2013) 025007.
- [40] J. Zhou, C. Li, M. Guan, F. Ren, X. Wang, S. Zhang, B. Zhao, Zener pinning by coherent particles: pinning efficiency and particle reorientation mechanisms, *Modelling Simul. Mater. Sci. Eng.* 25 (2017) 065008.
- [41] R.K. Koju, K.A. Darling, K.N. Solanki, Y. Mishin, Atomistic modeling of capillary-driven grain boundary motion in Cu-Ta alloys, *Acta Mater.* 148 (2018) 311–319.
- [42] B.C. Hornbuckle, T. Rojhirunsakool, M. Rajagopalan, T. Alam, G.P. Purja Pun, R. Banerjee, K.N. Solanki, Y. Mishin, L.J. Kecske, K.A. Darling, Effect of Ta solute concentration on the microstructural evolution in immiscible Cu-Ta alloys, *JOM* 67 (2015) 2802–2809.
- [43] B.C. Hornbuckle, K. Solanki, K.A. Darling, Prolonged high-temperature exposure: Tailoring nanocrystalline Cu-Ta alloys against grain growth, *Mater. Sci. Eng.: A* 824 (2021) 141818.
- [44] K.A. Darling, M. Rajagopalan, M. Komarasamy, M.A. Bhatia, B.C. Hornbuckle, R.S. Mishra, K.N. Solanki, Extreme creep resistance in a microstructurally stable nanocrystalline alloy, *Nature* 537 (2016) 378–381.
- [45] C. Kale, S. Srinivasan, S. Sharma, B.C. Hornbuckle, R.K. Koju, S. Grendahl, K. Darling, Y. Mishin, K. Solanki, Exceptional fatigue strength of a microstructurally stable bulk nanocrystalline alloy, *Acta Mater.* 255 (2023) 119049.
- [46] J. Weißmüller, Alloy thermodynamics in nano-structures, *J. Mater. Res.* 9 (1994) 4–7.
- [47] J. Weißmüller, Alloy effects in nanostructures, *Nanostruct. Mater.* 3 (1993) 261–272.
- [48] R. Kirchheim, Grain coarsening inhibited by solute segregation, *Acta Mater.* 50 (2002) 413–419.
- [49] F. Liu, R. Kirchheim, Nano-scale grain growth inhibited by reducing grain boundary energy through solute segregation, *J. Cryst. Growth* 264 (2004) 385–391.
- [50] R. Kirchheim, Reducing grain boundary, dislocation line and vacancy formation energies by solute segregation. I. Theoretical background, *Acta Mater.* 55 (2007) 5129–5138.

- [51] R. Kirchheim, Reducing grain boundary, dislocation line and vacancy formation energies by solute segregation. II. Experimental evidence and consequences, *Acta Mater.* 55 (2007) 5139–5148.
- [52] C.E. Krill, H. Ehrhardt, R. Birninger, Thermodynamic stabilization of nanocrystallinity, *Int. J. Mater. Res.* 96 (2005) 1134–1141.
- [53] L.S. Schwindlerman, G. Gottstein, Unexplored topics and potentials of grain boundary engineering, *Scr. Mater.* 54 (2006) 1041–1045.
- [54] J. Li, Y. Mishin, Line and planar defects with zero formation free energy: Applications of the phase rule toward ripening-immune microstructures, 2025, ArXiv preprint [arXiv:2505.24092](https://arxiv.org/abs/2505.24092).
- [55] O. Hussein, Y. Mishin, A model of thermodynamic stabilization of nanocrystalline grain boundaries in alloy systems, *Acta Mater.* 281 (2024) 120404.
- [56] F.Y. Wu, The potts model, *Rev. Modern Phys.* 54 (1982) 235–268.
- [57] G.H. Vineyard, Frequency factors and isotope effects in solid state rate processes, *J. Phys. Chem. Solids* 3 (1957) 121–127.
- [58] I. Kaur, Y. Mishin, W. Gust, *Fundamentals of Grain and Interphase Boundary Diffusion*, Wiley, Chichester, West Sussex, 1995.
- [59] I. Chesser, R.K. Koju, Y. Mishin, Atomic-level mechanisms of short-circuit diffusion in materials, *Int. J. Mater. Res.* 115 (2024) 85–105.
- [60] A.B. Bortz, M.H. Kalos, J.L. Lebowitz, A new algorithm for monte carlo simulation of ising spin systems, *J. Comput. Phys.* 17 (1975) 10–18.
- [61] M.I. Mendelev, D.J. Srolovitz, W. E, Grain-boundary migration in the presence of diffusing impurities: simulations and analytical models, *Phil. Mag.* 81 (2001) 2243–2269.
- [62] M.I. Mendelev, D.J. Srolovitz, Kink model for extended defect migration in the presence of diffusing impurities: theory and simulation, *Acta Mater.* 49 (2001) 2843–2852.
- [63] J.M. Liu, Monte carlo simulation of solute aggregation on domain boundaries in binary alloys: Domain-boundary segregation and domain growth, *Phys. Rev. B* 58 (1998) 633–640.
- [64] J.M. Liu, L.C. Lim, Z.G. Liu, Monte carlo simulation of solute aggregation in binary alloys: Domain boundary precipitation and domain growth, *Phys. Rev. B* 60 (1999) 7113–7126.
- [65] K. Binder, Static and dynamic critical phenomena of the two-dimensional q-state Potts model, *J. Stat. Phys.* 24 (1981) 69–86.
- [66] X. Chen, F. Liu, S. Chen, J. Shen, W. Deng, G. Papp, W. Li, C. Yang, Study of phase transition of Potts model with Domain Adversarial Neural Network, *Phys. A* 617 (2023) 128666.
- [67] V. Beffara, H. Duminil-Copin, The self-dual point of the two-dimensional random-cluster model is critical for $q \geq 1$, *Probab. Theory Related Fields* 153 (2012) 511–542.
- [68] A.R. Kalidindi, T. Chookajorn, C.A. Schuh, Nanocrystalline materials at equilibrium: A thermodynamic review, *JOM* 67 (2015) 2834–2843.